

Three dimensional reconstructions from low-count SPECT data using deformable models

G.S. Cunningham,¹ K.M. Hanson¹ and X.L. Battle²

¹MS P940, Los Alamos National Laboratory, Los Alamos, NM 87545 USA

²Faculte de Medecine, Universite de Bretagne Occidentale, 29200 Brest, FR

Abstract

We demonstrate the reconstruction of a 3D, time-varying bolus of radiotracer from first-pass data obtained at the dynamic SPECT imager, FASTSPECT, built by the University of Arizona. The object imaged is a CardioWest Total Artificial Heart. The bolus is entirely contained in one ventricle and its associated inlet and outlet tracts. The model for the radiotracer distribution is a time-varying closed surface parameterized by 162 vertices that are connected to make 960 triangles, with uniform intensity of radiotracer inside. The total curvature of the surface is minimized through the use of a weighted prior in the Bayesian framework. MAP estimates for the vertices, interior intensity and background scatter are produced for diastolic and systolic frames, the only two frames analyzed. The strength of the prior is determined by finding the corner of the L-curve. The results indicate that qualitatively pleasing results are possible even with as few as 1780 counts per time frame (total after summing over all 24 detectors). Quantitative results will require correcting certain undesirable features of the reconstruction due to inappropriate assumptions in the model, e.g. inhomogeneities in the radiotracer distribution and smoothness of the surface at the tract/ventricle join.

I. INTRODUCTION

The FASTSPECT imaging system [1], developed at the University of Arizona, has been used for first-pass tomographic imaging of the time-varying distribution of a bolus of Tc-99m radiotracer infused into a CardiacWest Total Artificial Heart. A voxel-based reconstruction can be generated from the data, using e.g. the ML-EM method, and regions of interest can be manually defined to derive estimates of the ventricular volumes as a function of time. These time-history curves can ultimately be reduced to ejection fraction, a simple indicator of heart function. In contrast to the voxel-based approach, one can solve the reconstruction problem by directly estimating from the raw projection data the time-varying parameters of a geometric model inside of which some simple parameterized model for the distribution of radiotracer is assumed [2-4]. In this article we formulate a Bayesian estimation problem for first-pass tomographic imaging using FASTSPECT that directly estimates the time-varying (x,y,z) components of the vertices of a triangulated surface within which it is assumed the bolus is uniformly distributed [5-6]. If the bolus is indeed homogeneously mixed within a ventricular volume of interest, then the estimated surface provides an estimate of the ventricular volume, and

ultimately ejection fraction, but it also provides a great deal more information of potential clinical value, since the entire interior surface of the ventricle is revealed.

In this article, we first describe the FASTSPECT imaging system and the real data that were analyzed. Next we formulate the Bayesian estimation problem and, finally, we present some results and conclusions.

II. THE DATA

A. FASTSPECT

FASTSPECT is a dynamic SPECT imager that has been used for brain, heart and bone imaging [1]. Two circular arrays with a total of 24 pinhole apertures surround the volume of interest. Each pinhole is mapped to an Anger detector, and the voltages from the 4 photomultipliers that see a monolithic scintillating crystal for each detector are converted to an estimate of the position of each detected photon that must lie on a 64x64 uniformly-binned image grid. This detection system may eventually be replaced with a semiconductor-based system [7].

Pinholes of various diameter can be inserted into the dome surrounding the object volume; 2.5 mm diameter pinholes were used to generate the data analyzed in this article. The system is characterized by a matrix \mathbf{H} that is measured by passing a small volume element of radiotracer throughout the volume being imaged, and measuring the response of every detector pixel element to that source, producing an enormous amount of information, even when compressed to take advantage of the sparsity of the matrix (150 MB of disk space after compression). The system matrix used in this article was obtained by passing a [5mm]³ volume element through a 43x57x39 grid. The system matrix is noisy, since only a finite number of counts are obtained for each location of the source. Given enough patience and time, though, this noise could presumably be made as low as is needed. If information is available concerning attenuating material between the radiotracer distribution and the pinholes, it can easily be incorporated into the \mathbf{H} matrix, and this was done for the system matrix used to analyze the data discussed in this article.

B. The imaged object and raw data

The object that was imaged is a CardioWest Total Artificial Heart. This device consists of a left and right ventricle, each about 120 ml, and two atria. A 10-20 mCi bolus of Tc-99m was infused and the first-pass diastolic and

systolic frames were analyzed. The diastolic frame (Fig 1a) contained a total of 2133 counts, of which approximately 40 appear to be scattered photons. The systolic frame (Fig 1c) contained a total of 1780 counts, with a similar number of scattered photon events.

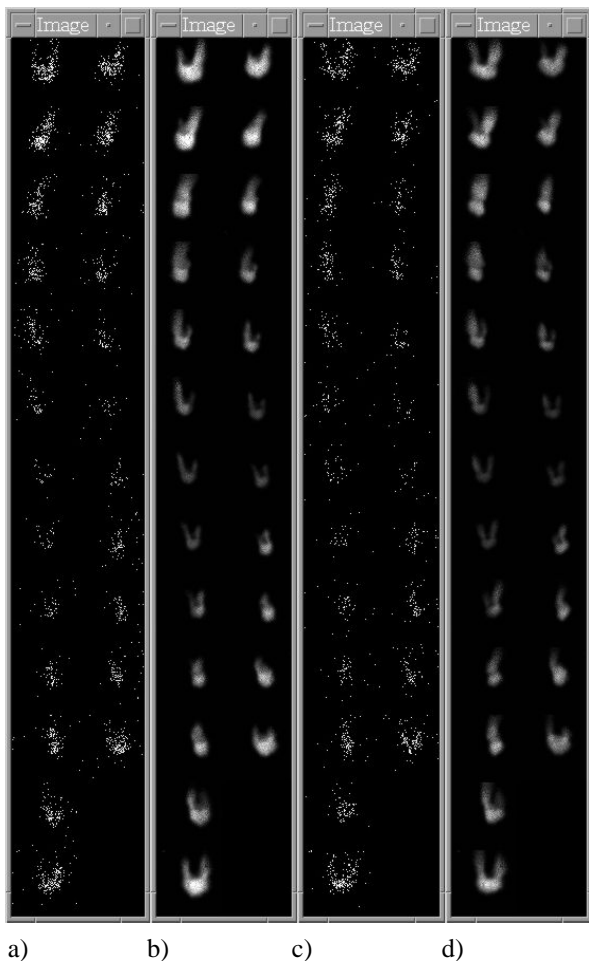


Figure 1. Raw data for a) diastolic frame and c) systolic frame. Predicted detector Poisson rates for b) diastolic frame and d) systolic frame using MAP solution with $\alpha=0.2$.

III. THE BAYESIAN ESTIMATION PROBLEM

We have implemented a general tool for Bayesian estimation in the context of image analysis using geometric models that we call the Bayes Inference Engine (BIE). We conceive of the Bayesian estimation problem as consisting of three parts: the object model, the measurement model, and the probability model. In the BIE, the user constructs a graphical program that transforms object and measurement system parameters into predicted data. The predicted data is compared with real data to produce a log-probabilistic goal function, and an optimizer is connected to goal function and any parameters that are to be estimated by minimizing the goal function. See Figure 2 for the graphical program that was used to analyze the data discussed in this article.

A. The object model

The object model is the parametric model of whatever spatio-temporal physical quantity we are interested in; in this case, it is the parametric model for the 3D(t) radiotracer intensity distribution. In the BIE, we always convert parametric models to non-parametric ones (uniformly sampled grids) so that more complex models can easily be built through

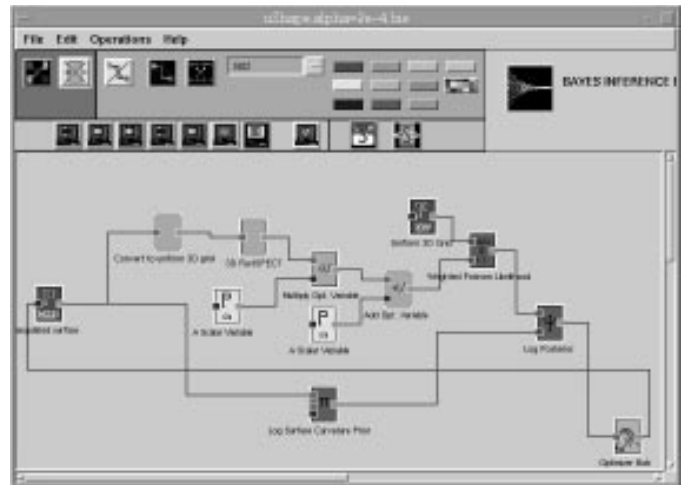


Figure 2. BIE canvas used to analyze SPECT data.

combination with other models. The parametric model we use here is a triangulated surface that evolves in time, defined by a set of 162 vertices (x,y,z) , and a connectivity network that creates 960 triangles by connecting vertices together. Since the (x,y,z) for every vertex at each time must be estimated, there are 486 parameters for this part of the model at each time. We assume that the radiotracer is homogeneously distributed throughout the volume enclosed by the triangulated surface, so that only a single parameter is needed for the activity level. More complicated models for the 3D distribution are easily accommodated in the BIE, e.g. a voxelated grid of values with lower and upper bounds or an unconstrained voxelated grid with an associated prior penalizing high-frequency variations.

B. The measurement model

The measurement model uses as input a nonparametric version of the object model, call it \mathbf{f} , and produces a set of predicted data elements, \mathbf{g} , in this case a Poisson rate for each detector pixel. The measurement model might in general contain many components, e.g. in an x-ray radiographic system, one would expect to have line integral transformations (parallel- or divergent-beam), convolutions, exponential point transforms, etc.

For the FASTSPECT machine, though, the measurement model is merely \mathbf{H} , along with a single additive constant that models the scatter background (the same background constant is used for all 24 detectors), so that $\mathbf{g}=\mathbf{H}\mathbf{f}+\mathbf{s}$. The scatter background \mathbf{s} must be jointly estimated from the data along with the object model parameters. Much more complicated 2D spatial field models exist within the BIE, but the very low number of scattered photon counts probably make more complex models impossible to estimate well. One extension that is worth investigating is a different scatter offset for each detector that varies in time in a plausible way.

The nature of our object model allows us to speed up the calculation \mathbf{Hf} dramatically since only a few percent of the voxels in the object model are nonzero. Simply skipping over \mathbf{Hf} for values of \mathbf{f} that are zero allows us to calculate \mathbf{Hf} in about 300 msec on a DEC Alpha 500/500. The same applies in the adjoint direction, wherein derivatives are propagated according to the chain rule in the direction opposite of the path direction that transforms object parameters into predicted data [8].

C. The probability model

The probability model for the object penalizes a discrete approximation to the local curvature at every edge shared by two triangles on the surface in order to enforce smoothness of the estimated surface. Let \mathbf{n}_i be the normal to the i^{th} triangle. We define θ_{ij} to be the angle between \mathbf{n}_i and \mathbf{n}_j . Then, if A_i is the area of the i^{th} triangle, and l_{ij} is 1/3 the height of the i^{th} triangle relative to the edge shared by triangles i and j , the curvature prior is defined as

$$\pi(\mathbf{x}) = \sum_i A_i (\sum_j [\tan(\theta_{ij}/2) / l_{ij}]^2) \quad (1)$$

where i indexes over all triangles on the surface and j indexes over all triangles that share an edge with the i^{th} triangle.

The form in (1) is slightly different from the form we used during our first attempts to analyze simulated FASTSPECT data [5,6]. First, the tangent-squared term in (1) is divided by a length over which it is assumed that half the angular difference occurred [9]. As the angle gets small, the total term looks like an angular velocity w.r.t. arclength, which is the definition of curvature for a curve. Note that this term is not symmetric in the triangles i and j , and that we did not use a simpler definition for l_{ij} that calculates the distance from the midpoint of one triangle to the midpoint of the shared edge. These subtleties are intentional, and may be important in keeping the triangulation evenly distributed on the surface during the course of the gradient-based optimization so that no remeshing of the surface is needed. Second, the total surface area no longer appears in the denominator in (1). This is also intentional since such a term would make the prior favor larger surfaces (with the new numerator definition).

The definition in (1) is invariant to isotropic scale changes in the object and also to the number of triangles used in the discrete representation of the surface, as long as the angles are small. This could be an important feature if re-meshing is needed, since one can easily re-mesh to a new set of triangles that does not affect the value of the prior, if all of the angles are small.

The probability model for the likelihood is the Poisson distribution with mean value equal to the predicted data (predicted detector pixel Poisson rates, \mathbf{g}) and count values equal to the raw data:

$$\begin{aligned} \phi(\mathbf{x}) &= -\ln \text{Prob}[\text{data}/\text{predicted data}] \\ &= \sum_i [-k_i \ln g_i + g_i] \end{aligned} \quad (2)$$

where we have ignored terms in (2) that depend only on the data \mathbf{k} . The dependence of the predicted data \mathbf{g} on the underlying parameters \mathbf{x} is understood. Note that because of the additive background scatter constant in the measurement

model, the predicted detector pixel rates \mathbf{g} can never be equal to or less than zero as long as the activity level and scatter level are greater than or equal to zero, which makes the form in (2) well-defined, and makes the derivative of (2) w.r.t. \mathbf{g} (and ultimately \mathbf{x}) well-behaved.

C. The estimation problem

The Bayesian estimation problem is to find the values for the object and measurement system model parameters \mathbf{x} that produce the maximum *a posteriori* (MAP) probability, or the minimum minus log posterior:

$$\mathbf{x}^{\text{MAP}}(\alpha) = \arg \min_{\mathbf{x}} [\phi(\mathbf{x}) + \alpha \pi(\mathbf{x})] \quad (3)$$

for some fixed value of the hyperparameter α . The higher-order problem is to determine the value of α from the data. The Bayesian solution to the higher-order problem is to determine the α that yields the greatest evidence for the data, where the evidence is the marginal over the joint posterior distribution of parameters and data (leaving just the probability of the data, called the evidence) [10]. However, evaluation of the evidence is computationally nontrivial, so for now we use an alternative, heuristic approach.

We determine α using the L-curve [11], the continuum of 2D points

$$(\phi(\mathbf{x}^{\text{MAP}}(\alpha)), \pi(\mathbf{x}^{\text{MAP}}(\alpha))) \quad (4)$$

parameterized by α . The L-curve approach is traditionally used for linear least-squares with quadratic regularization, but, to the degree that the minus log posterior is quadratic, an L-curve approach might be reasonable.

The value of α chosen for the final estimate is the one that yields the point on the L-curve that is closest to the ‘‘corner’’. For very large values of α , the MAP solution is over-regularized. As α decreases, much better fits to the data are allowed (decreasing minus log likelihood) at very little cost to the prior. This is the vertical line part of the L-curve (Figure 3). For small values of α , the MAP solution is under-regularized, and the data is well-fit (small value of minus log likelihood). Now, very large increases in the minus log prior are needed to allow sufficient freedom in the model so that any decrease in the minus log likelihood can result. This is the horizontal line part of the L-curve (Figure 3). Obviously, we’d like to choose an α that is somewhere between these two extremes, thus the ‘‘corner’’ criterion. A value of $\alpha=0.2$ produces a point on the L-curve that is approximately halfway between the endpoints of the two extreme regions just described and yields a qualitatively pleasing result.

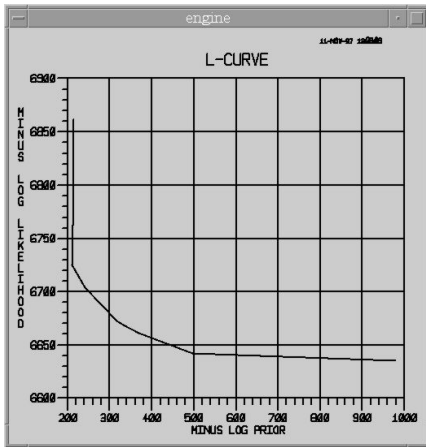


Figure 3. The L-curve for the diastolic frame.

IV. RESULTS

The MAP solutions for a range of α using the data in Figure 1a (diastolic frame) are shown in Figure 4. As discussed above, large values of α produce over-regularized MAP solutions, while small values of α produce under-regularized, noisy solutions. The MAP solution using $\alpha = 0.2$ is chosen as the best MAP estimate. This value of α was used to find the MAP solution for the data in Figure 1c (systolic frame).

Comparison between the MAP reconstructions of the bolus boundary for the diastolic and systolic frames (see Figures 5 and 6) shows the type of behavior that we expect in most regions. The inlet tract shows very little change in distribution between diastolic and systolic frames presumably because the valve

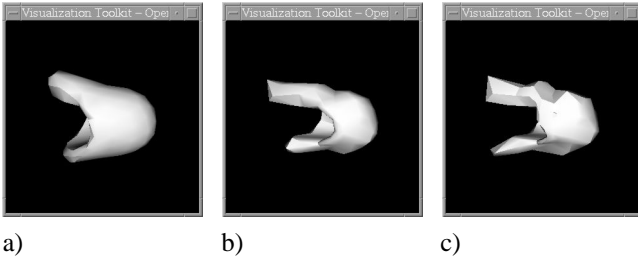


Figure 4. MAP reconstructions of the bolus boundary surface using a) $\alpha=3.2$, b) $\alpha=0.2$, and c) $\alpha=0.1$.

that regulates flow between the tract and the ventricle is closed during that time (Figure 5a-b and 6a-d, top tube). The diaphragm at the bottom of the ventricle moves toward the inlet and outlet tracts, as expected, causing the ventricular volume to decrease in that region (Figure 5a and 6d-e, right side). The bolus boundary expands along the direction of blood flow through the outlet tract (Figure 5b and 6b-f, bottom tube).

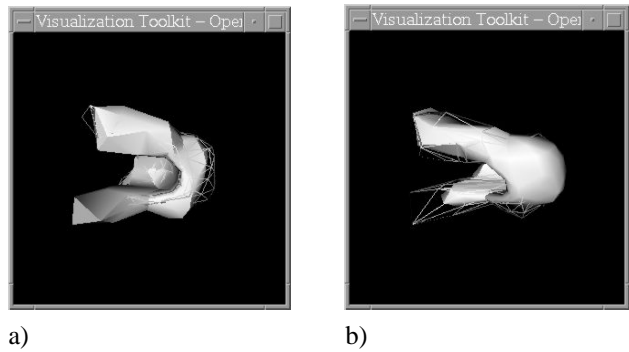


Figure 5. Comparison between diastolic and systolic frame reconstructions: a) diastolic frame is wireframe and systolic frame is solid surface, b) diastolic frame is solid surface and systolic frame is wireframe.

There are several features of the reconstructions that are bothersome, however. The bolus boundary appears to expand rather than contract within the ventricular volume on the side closest to the outlet tube during the transition from diastoli to systoli (Figure 5b and 6f, bottom right). This feature tends to make the apparent ventricular volume increase from diastoli to systoli, rather than decrease, in that region. This problem could be due to inhomogeneity in the mixing of the radiotracer. If the inhomogeneity is not severe, then simple low-frequency models for spatial distribution of the radiotracer within the surface might be able to eliminate this feature and result in a surface estimate at systoli that is nearer to the ventricular wall. Another puzzling feature of the reconstructions is the ring connecting the two tracts that lies on top of one side of the ventricle (Figure 4b, back surface of ventricle between the two tubes). This feature may be an artifact of the curvature prior since there is a high-curvature region that connects the tubes to the ventricles whose true configuration may be disallowed by the prior. This feature might be eliminated if the curvature prior were de-weighted at the join between tube and ventricle, allowing a “kink” to develop at the join [9]. Until these features are eliminated, an estimate of the time-varying volume and ejection fraction using the model proposed in this article would be imprecise, and so it is not attempted.

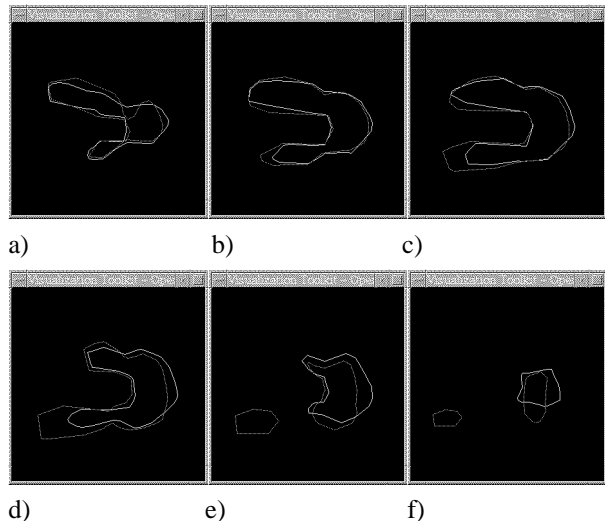


Figure 6. Cut planes through the reconstructions in Figure 5. Thick lines are for diastolic frame and thin lines are for systolic frame. Z-slices are a) -8 mm, b) -4 mm, c) 0 mm, d) 4 mm, e) 8 mm, and f) 12 mm.

V. CONCLUSIONS

We have formulated the analysis of very low-count, first-pass cardiac SPECT data in a Bayesian framework using deformable geometric models. In particular, the model used assumes that the radiotracer distribution within the tracts and ventricle is uniformly distributed inside a volume defined by a closed, triangulated surface with 162 vertices and 960 triangles. We jointly estimate the intensity of the distribution as well as the positions of the vertices of the surface from the raw data. We use the system matrix for FASTSPECT and an unknown constant additive background to model the predicted rates at the detector as a function of volumetric distributions of radiotracer parameterized by the surface. The system matrix and raw data were provided to us by the University of Arizona. The raw data consists of 24 pinhole views of the distribution at diastoli and systoli, with a total count level (integrated over all 24 detectors) of 2133 and 1780 at diastoli and systoli, respectively.

The results indicate the enormous potential for deformable geometric models in the context of first-pass cardiac SPECT data, but several features of the reconstructions must be understood and corrected before quantitative estimates of volume can be obtained. In the near future we anticipate correcting the undesirable features of the reconstructions by expanding the capability of the model to include surface "kinks" and 3D low-frequency spatial variation of the radiotracer distribution within the surface. We also plan to create truly time-evolving models for the radiotracer distribution that use priors on the spatio-temporal nature of the surface velocity field.

VI. ACKNOWLEDGMENTS

This work was supported by the U.S. Department of Energy under contract 7405-ENG-36. We thank Irene Pang and Harry Barrett of the University of Arizona for supplying us with the FASTSPECT data and associated system matrix.

VII. REFERENCES

[1] W.P. Klein, H.H. Barrett, I. W. Pang, D.D. Patton, M.M. Rogulski, and J.J. Sain, "FASTSPECT: Electrical and mechanical design of a high resolution dynamic SPECT imager," Conference Record of the 1995 IEEE Nucl. Sci. Symp. & Med. Imaging Conf. **2**, pp. 931-933, 1996.

[2] K.M. Hanson, "Bayesian reconstruction based on flexible prior models," *J. Opt Soc. Amer. A* **10**, pp. 997-1004, 1993.

[3] Y. Bresler, J.A. Fessler, and A. Macovski, "A Bayesian Approach to reconstruction from incomplete projections of a multiple object 3D domain," *IEEE Trans. Pattern Anal. Mach. Intell.*, **11**, pp. 840-858, 1989.

[4] P.C. Chiao, W.L. Rogers, N.H. Clinthorne, J.A. Fessler, and A.O. Hero, "Model-based estimation for dynamic cardiac studies using ECT," *IEEE Trans. Med. Imaging*, **13**, pp. 217-226, 1994.

[5] X.L. Battle, G.S. Cunningham, and K.M. Hanson, "3D tomographic reconstruction using geometrical models," *Proc. SPIE* **3034**, pp. 346-357, 1996.

[6] X.L. Battle, G.S. Cunningham, and K.M. Hanson, "Tomographic reconstruction using 3D deformable models," to appear in *Physics in Med. Biol.*, submitted Oct 1997.

[7] <http://www.radiology.arizona.edu/~fastspec/detectors.html>

[8] K.M. Hanson, "A computational approach to Bayesian inference," M.M. Meyer and J.L. Rosenberger, eds., *Computing Science and Statistics* **27**, pp. 202-211. Interface Foundation, Fairfax Station, VA 22039-7460, 1996.

[9] K.M. Hanson, R.L. Bilisoly, and G.S. Cunningham, "Kinky tomographic reconstruction," *Proc. SPIE* **2710**, pp. 156-166, 1996.

[10] D.J.C. MacKay, "Bayesian interpolation," *Neural Computation* **4**, pp. 415-447, 1992.

[11] P.C. Hansen and D.P. O'Leary, "The use of the L-curve in the regularization of discrete ill-posed problems," *SIAM J. Sci. Comput.*, **14**, pp. 1487-1503, 1993.